

ARTICLE

<https://doi.org/10.1038/s42005-019-0222-9>

OPEN

Engineering medium-range order and polyamorphism in a nanostructured amorphous alloy

Si Lan ^{1,2}, Chunyu Guo¹, Wenzhao Zhou³, Yang Ren⁴, Jon Almer ⁴, Chaoqun Pei¹, Horst Hahn ^{1,5}, Chain-Tsuan Liu⁶, Tao Feng^{1*}, Xun-Li Wang ^{2,7*} & Herbert Gleiter^{1,5}

Like crystalline materials, the properties of amorphous materials can be tailored by tuning the local atomic-to-nanoscale structural configurations. Polyamorphism is evident by the coexistence of kinetically stabilized amorphous structures with tailorable short-to-medium-range orders, providing a viable means to engineer the degree of local order and heterogeneity. Here, we report experimental evidence of the coexistence of liquid-like and solid-like amorphous phases in a Ni₈₂P₁₈ amorphous alloy with enhanced thermal stability and plasticity prepared by pulsed electrodeposition. The two amorphous phases, of comparable volume fraction of ~50% each, have similar short-range order but are distinguished by packing at the medium-range length scale (>6 Å). Upon heating, a structure crossover at ~450 K was observed, where the liquid-like structure transforms to the solid-like structure, as evidenced by the enthalpy release and an anomalous contraction of atomic structure over the medium-range length scale, due to the metastable nature of the liquid-like structure.

¹Herbert Gleiter Institute of Nanoscience, School of Materials Science and Engineering, Nanjing University of Science and Technology, 200 Xiaolingwei Avenue, Nanjing 210094, China. ²Department of Physics, City University of Hong Kong, 83 Tat Chee Avenue, Kowloon, Hong Kong SAR, China. ³Centre for Advanced Structural Materials, City University of Hong Kong, Shenzhen Research Institute, 8 Yuexing 1st Road, Shenzhen Hi-Tech Industrial Park, Nanshan District, Shenzhen 518057, China. ⁴X-ray Science Division, Argonne National Laboratory, Argonne IL 60439, USA. ⁵Institute of Nanotechnology, Karlsruhe Institute of Technology (KIT), 76021 Karlsruhe, Germany. ⁶Center for Advanced Structural Materials & Department of Materials Science and Engineering, City University of Hong Kong, 83 Tat Chee Avenue, Kowloon, Hong Kong SAR, China. ⁷Center for Neutron Scattering, City University of Hong Kong, Shenzhen Research Institute, 8 Yuexing 1st Road, Shenzhen Hi-Tech Industrial Park, Nanshan District, Shenzhen 518057, China. *email: tao.feng@njust.edu.cn; xlwang@cityu.edu.hk

The structure of amorphous materials is characterized by disorder on the long-range length scale but by local order at short-range to medium-range length scales^{1–4}. This complexity has led to some ambiguities in describing these structures, particularly for evolving structures during phase transitions, e.g., glass transitions^{1,5}. To modify the properties of amorphous materials, it is desirable to develop the ability to tailor the local order in disordered states^{6,7}. However, the structure factor for glassy alloys prepared using conventional methods, i.e., rapid quenching techniques^{8,9}, usually looks the same: beyond the first sharp diffraction peak, there are several peak maxima propagated at a limited momentum transfer, Q ($5\text{--}20\text{ \AA}^{-1}$)^{10,11}. Moreover, there is often a right shoulder peak with lower intensity for the second peak maximum^{12,13}, indicating the short-to-extended range structural order. Tailoring local order based on the temperature parameter in amorphous states is difficult due to the fast critical quenching rate for most metallic glass (MG) alloy systems^{7,14}.

Before the first rapidly quenched glassy alloy was reported in 1960¹⁵, electrodeposition (ED) had already been employed as a powerful technique for preparing metastable alloys¹⁶. The ED amorphous alloys, e.g., the iron-group alloys¹⁷, which are similar to thermally synthesized alloys in structure, have been widely used in electronics applications, such as in computers, space technology, and energy storage devices, due to their attractive magnetic, mechanical, and chemical properties^{16–19}. Pulsed ED has been successfully used to prepare Ni–P amorphous alloys^{20,21}. The reported ED Ni–P amorphous alloys possessed similar diffraction patterns^{22,23} as that of the MGs but showed nanoscale structure inhomogeneity. The different regions in the ED Ni–P are characterized by different chemical compositions or packing densities. Presumably, if one can obtain ED Ni–P amorphous alloys of dual phases with appropriate volume fractions by, for example, changing the parameters during deposition, it could be possible to tailor the packing scheme at medium-range order (MRO) in the amorphous state. Those changes in microstructure would be manifested in the structure factor, which can be determined using diffraction measurements.

Polyamorphous phase transitions (PPTs), including amorphous solid-to-solid (SS)^{24–27} phase transition, and liquid-to-liquid (LL) phase transition^{28–30}, are still a debated issue. A PPT has been proposed in a Ni₈₂P₁₈ glass upon heating^{23,31,32}. In this regard, the observation of coexisting multiple amorphous states at the same time and space^{33,34} would provide direct evidence for a PPT in amorphous alloys. That being the case, it would be possible to modify the local order in disordered materials by temperature or pressure-induced PPTs, which should lead to tailorable properties for amorphous materials, such as the thermal stability and mechanical properties⁷.

In this paper, we demonstrate that Ni₈₂P₁₈ amorphous alloys, prepared using multi-phase pulsed ED within a specific pulse current range²⁰, have a unique structure factor: for the second peak maximum, there are two sub-peaks with comparable diffraction intensities. The ED Ni₈₂P₁₈ amorphous alloys consist of the following two kinds of amorphous structural components: nanometer-sized regions with solid-like structure (SLS, the atomic structure of melt-quenched MG-like Ni₈₂P₁₈) and nanometer-sized regions with liquid-like structure (LLS, of loose-packing compared to a melt-quenched Ni–P ribbon sample). The structure of the ED Ni₈₂P₁₈ amorphous alloy was determined using transmission electron microscopy (TEM) and high-energy synchrotron X-ray scattering. The composition distribution was characterized by atom probe tomography (APT). Real-space analysis, via pair distribution function (PDF), indicates that the loose-packing regions in ED Ni₈₂P₁₈ alloys have larger atomic spacing over the medium-range length scale ($\sim 6\text{ \AA}$), which is

consistent with the features of the difference between liquid and glassy states for two excellent glass-forming alloys, Zr₅₇Nb₅Al₁₀–Cu_{15.4}Ni_{12.6} (Vit 106) and Pd₄₃Cu₂₇Ni₁₀P₂₀, respectively. Simultaneous small-angle/wide-angle X-ray scattering (SAXS/WAXS) reveal a ‘solidification-like’ structure transformation of the ED Ni₈₂P₁₈ alloy upon heating. Finally, compared with the expansion behavior of MG Ni₈₂P₁₈ alloys, an unusual thermal contraction at medium-range length scale for the LLS of the ED Ni₈₂P₁₈ alloy is demonstrated by PDF analysis. The thermal mechanical analysis (TMA) measurements revealed an anomalous change in the coefficient of thermal expansion (CTE) for ED Ni₈₂P₁₈ alloy upon heating, further confirming a PPT at $\sim 450\text{ K}$. Furthermore, the as-prepared ED Ni₈₂P₁₈ amorphous alloys show better thermal stability and even tensile ductility at the sub-micron scale.

Results

Thermal analysis and nanoscale heterogeneity. Figure 1a presents the differential scanning calorimetry (DSC) scans for the as-prepared MG Ni₈₂P₁₈ ribbons and ED Ni₈₂P₁₈ amorphous alloys. The ED Ni₈₂P₁₈ was prepared using the highest pulse current density (400 mA cm^{-2}) to introduce a different structure. Supplementary Fig. 1 shows the $S(Q)$ patterns for ED Ni₈₂P₁₈ samples prepared at different pulse current densities. The crystallization temperature T_{X2} for the ED Ni₈₂P₁₈ alloy is $\sim 633\text{ K}$, which is $\sim 53\text{ K}$ higher than that of the MG Ni₈₂P₁₈ alloy ($T_{X1} \sim 580\text{ K}$). Surprisingly, there is a thermal release phenomenon at T_S , $\sim 450\text{ K}$, for the ED Ni₈₂P₁₈ alloy, which is much lower than the nominal glass transition temperature (T_g), $\sim 570\text{ K}$, for the MG Ni₈₂P₁₈ sample³⁵. The calorimetric studies suggest that there might be a structural change upon heating and the ED Ni₈₂P₁₈ alloy has much better thermal stability than that of the MG Ni₈₂P₁₈ alloy. The APT results in Fig. 1b illustrate the uniform distribution of the alloying elements (Ni and P) in the as-deposited ED Ni₈₂P₁₈ alloy. Figure 1c is the high angle annular dark field (HAADF) image acquired in scanning transmission electron microscopy (STEM) mode for the ED Ni₈₂P₁₈ alloy. It shows variations of mass/thickness contrast $\sim 10\text{--}20\text{ nm}$, indicating that the microstructure of the ED Ni₈₂P₁₈ alloy varies on a nanometer scale. The inset in Fig. 1c is the selective area electron diffraction (SAED) pattern, which illustrates that the sample is amorphous, with diffuse halos. Figure 1d, e display the HRTEM images for the dark and bright regions in Fig. 1c, showing typical maze-like amorphous structures. No distinct composition fluctuations were detected on the nanometer scale in the energy-dispersive X-ray spectroscopy (EDS) mapping, as shown in Fig. 1f. For comparison, Supplementary Fig. 2 illustrates the structural homogeneity using TEM observation for the MG Ni₈₂P₁₈ sample with the same chemical composition.

Figure 2a shows the SAXS profiles for the ED Ni₈₂P₁₈ alloy and the MG Ni₈₂P₁₈ ribbon. A hump at $\sim 0.02\text{ \AA}^{-1}$ in the SAXS log–log plot of the ED Ni–P sample confirms the presence of nanoscale structures in the ED sample. The model fitting result was obtained based on a simple hard-sphere model. The inset in Fig. 2a shows the intensity variation of SAXS profile for ED Ni₈₂P₁₈, which is much higher than that of the MG Ni₈₂P₁₈ ribbon sample, suggesting a much stronger scattering contrast for the scattering units in the ED sample. The SAXS profile of the MG alloy is nearly non-existent, suggesting a homogeneous structure (see Supplementary Fig. 2). On the other hand, the SAXS profile of the ED alloy shows a hump at $Q \sim 0.02\text{ \AA}^{-1}$, indicating the presence of nanoscale heterogeneous structures. The SAXS data were analyzed by using the software package IRENA in Igor³⁶. A spheroid model with polydispersity was employed to fit the scattering profile of the ED alloys. Figure 2b displays the calculated size distribution for the ED sample based

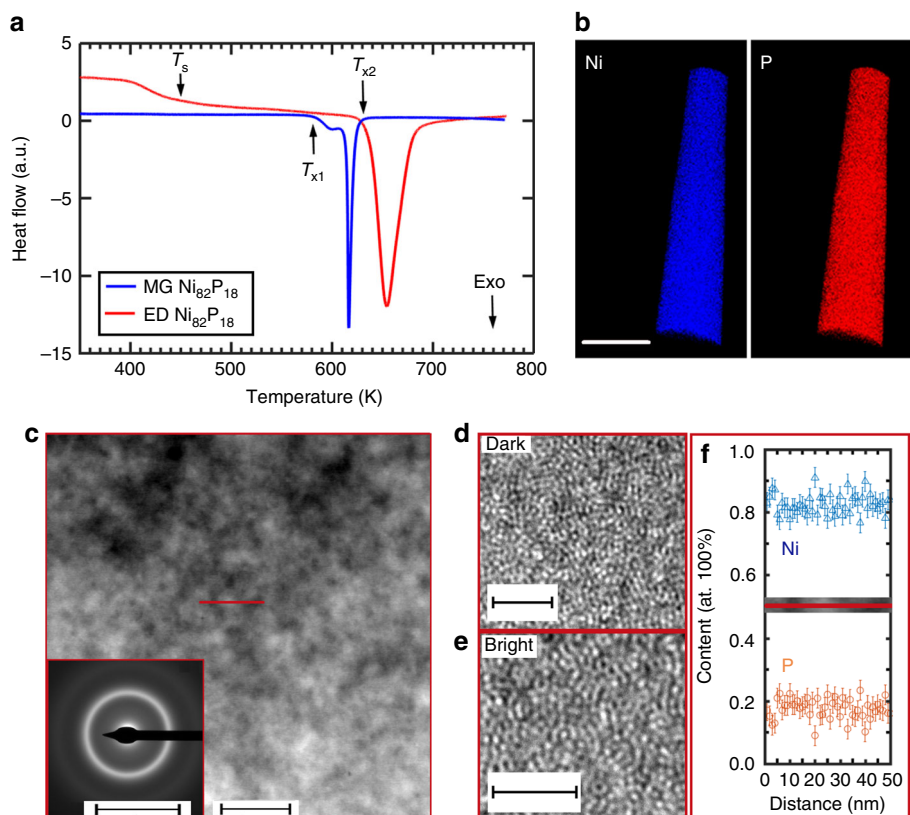


Fig. 1 Thermophysical behavior and structure inhomogeneity. **a** Calorimetric curves for metallic glass (MG) $\text{Ni}_{82}\text{P}_{18}$ ribbon (blue) and electrodeposition (ED) $\text{Ni}_{82}\text{P}_{18}$ alloy (red). **b** Composition mapping by 3D atomic probe, showing homogeneous Ni and P element distribution at nano-scale in ED $\text{Ni}_{82}\text{P}_{18}$ alloy; scale bar, 100 nm. **c** High angle annular dark field image (HAADF) of the ED $\text{Ni}_{82}\text{P}_{18}$ alloy, showing bright/dark contrast at 10–20 nm; scale bar, 50 nm. The inset is the selective area electron diffraction pattern (SAED) with diffused halos, illustrating the amorphous nature of the as-prepared ED $\text{Ni}_{82}\text{P}_{18}$ alloy; scale bar, 10 nm^{-1} . High-resolution transmission electron microscopy (HRTEM) images with the typical maze-like amorphous structure for the dark region **d** and bright region **e**. HAADF image; scale bars, 2 nm. **f** Energy-dispersive X-ray spectroscopy (EDS) line mapping results for Ni element and P element, showing that there is no obvious composition fluctuation. The average composition is Ni-82 at.% and P-18 at.%. The mapping line is indicated by the red line as shown in **c**. Error bars are defined as the standard deviation

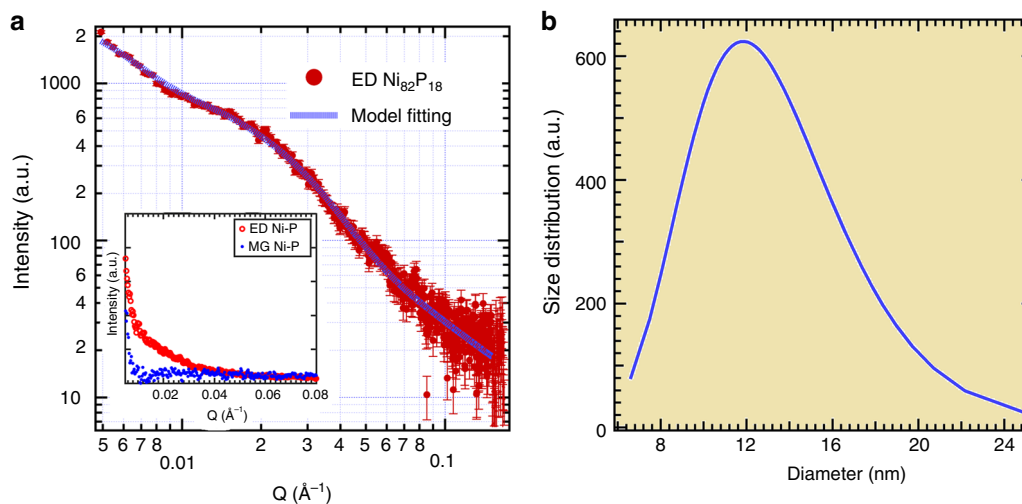


Fig. 2 Determination of heterogeneous nanoscale structure. **a** Small-angle X-ray scattering (SAXS) profiles for the electrodeposition (ED) $\text{Ni}_{82}\text{P}_{18}$ alloy and the metallic glass (MG) $\text{Ni}_{82}\text{P}_{18}$ ribbon. The blue dotted line is the model fitting based on the spheroid model with polydispersity. Error bars are defined as the standard deviation of photon count. For the inset, red circles and blue dots are SAXS profiles for ED alloy, MG ribbon plotted as linear scale respectively. **b** Size distribution function for ED $\text{Ni}_{82}\text{P}_{18}$ sample calculated by model fitting in **a**, showing that there are various regions with diameter ~8–25 nm

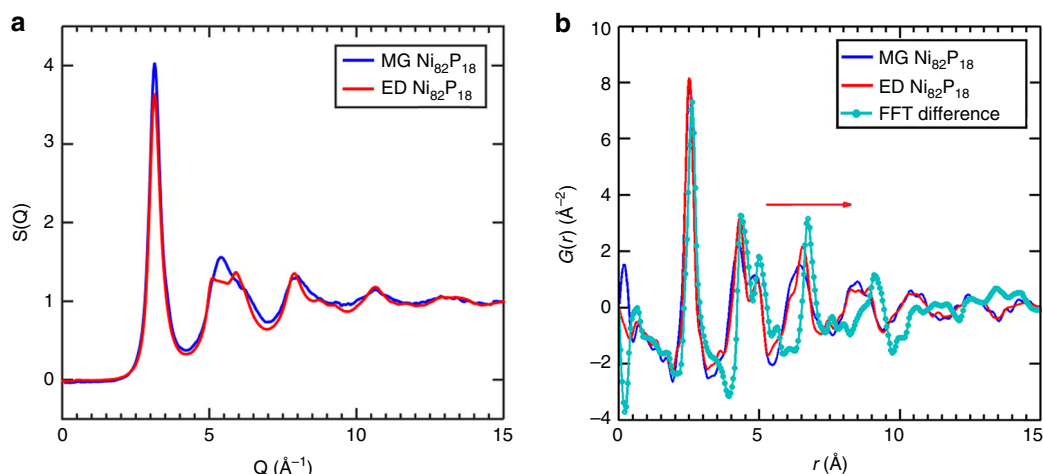


Fig. 3 Determination of the liquid-like structures. **a** Structure factor, $S(\mathbf{Q})$, for electrodeposition (ED) (red line) and metallic glass (MG) $\text{Ni}_{82}\text{P}_{18}$ (blue line) amorphous alloys. **b** Reduced pair distribution function (PDF), $G(r)$, for ED alloy (red line) and MG ribbon (blue line). The turquoise line with solid circles is the pattern obtained by fast Fourier transform (FFT) of the scaled difference $S(\mathbf{Q})$ between the ED alloy and ribbon. Details can be referred to the Supplementary Fig. 6 for FFT of the scaled difference $S(\mathbf{Q})$ pattern. The red arrow shows that there is a peak position shift in the sequence of MG $\text{Ni}_{82}\text{P}_{18}$ ribbon, ED $\text{Ni}_{82}\text{P}_{18}$, and the difference pattern

on the model fitting in Fig. 2a. It indicates that there are spheroidal granular-like structures with diameters distributed between 8 and 25 nm.

The existence of LLSs. Figure 3a shows the $S(\mathbf{Q})$ patterns of the ED and MG $\text{Ni}_{82}\text{P}_{18}$ amorphous alloys. The second peak maximum (Q range: $4.5\text{--}7.0\text{ \AA}^{-1}$) of the $S(\mathbf{Q})$ of the ED amorphous alloy shows two sub-peaks instead of the peak plus a shoulder in the ordinary $S(\mathbf{Q})$ pattern of MGs. As shown in Supplementary Fig. 3, the Rietveld refinement results of the diffraction patterns for the ED and MG alloys after crystallization illustrate that there are two crystalline products, Ni (space group: Fmmm) and Ni_3P (space group: I4), with almost the same weight percentage. Moreover, Supplementary Fig. 4 shows the $S(\mathbf{Q})$ patterns of MG and ED alloys before and after crystallization. The peak positions for the crystalline products were superimposed. There are sharp diffraction peaks in $S(\mathbf{Q})$ patterns of the samples after crystallization, which are different from the diffraction patterns of the amorphous alloys. Figure 3b illustrates the differential reduced PDF pattern, $G(r)$, obtained by a fast Fourier transform (FFT) of the difference $S(\mathbf{Q})$, which was obtained from ED $\text{Ni}_{82}\text{P}_{18}$ alloy pattern after subtracting 50% of the MG $\text{Ni}_{82}\text{P}_{18}$ ribbon pattern. The formation of ED Ni-P amorphous alloys is proposed to consist of nucleation and growth of the amorphous nano-grains²⁰. The structural model³⁷ of nanostructured amorphous alloys assumes amorphous nano-grains regions and the interface regions between the nano-grains. The atomic structure of the amorphous nano-grains is MG-like while the boundaries between those nano-grains exhibit a reduced packing density, i.e., higher free volume. Therefore, the change of the diffraction patterns with that of the deposition parameters in Supplementary Fig. 1 should originate from the increase of the interfacial regions between the amorphous nano-grains. The fitting to the SAXS profile of the ED $\text{Ni}_{82}\text{P}_{18}$ alloy based on the Debye-Bueche (DB) random two-phase model³⁸ illustrates that the volume fraction of the loose-packing regions is $\sim 53\%$. For comparison, the volume fraction of the MG-like phase in ED alloy used for calculating the difference $S(\mathbf{Q})$ was estimated to be 50% based on the TEM observation and SAXS pattern fitting. For further details of the DB model fitting, the readers are referred to the Supplementary Note 1 and Supplementary Fig. 5. Furthermore, Supplementary Fig. 6

demonstrates that a fluctuation in volume fraction within $\pm 10\%$ would not affect the outcome of the differential $G(r)$.

Figure 3b shows that the PDF peaks for the MG-subtracted pattern shift to a higher value beyond $r \sim 6\text{ \AA}$ (as indicated by an arrow), suggesting a MRO with larger atomic spacing. From the comparison of the peak positions of the calculated pattern with those of the MG sample, it can be seen that the first coordination shell changes little. However, the third coordination shell shifts by $\sim 2.30\%$. It is noted that the position ($6.5\text{--}6.7\text{ \AA}$) of the third coordination shell of the MG-subtracted pattern is similar to the position ($\sim 6.6\text{ \AA}$) of the third coordination shell of the $\text{Ni}_{81}\text{P}_{19}$ metallic liquid³⁹. To understand the significance of this increase, the peak positions for the third coordination shell of two representative metallic glass-forming liquids (MGFLs) and their glassy state counterparts: $\text{Zr}_{57}\text{Nb}_5\text{Al}_{10}\text{Cu}_{15.4}\text{Ni}_{12.6}$ (Vit 106) and $\text{Pd}_{43}\text{Cu}_{27}\text{Ni}_{10}\text{P}_{20}$ were determined. For both alloys, the first coordination shell changes only slightly, but the higher coordination shells shift significantly. As shown in Supplementary Fig. 7, the calculated differences of the third coordination shells, between liquid and glassy states, are 2.33% and 2.26%, respectively, for $\text{Zr}_{57}\text{Nb}_5\text{Al}_{10}\text{Cu}_{15.4}\text{Ni}_{12.6}$ (i.e., Vit 106) and $\text{Pd}_{43}\text{Cu}_{27}\text{Ni}_{10}\text{P}_{20}$. The above results provided evidence for the existence of a LLS with a different MRO in the ED Ni-P alloy.

Polyamorphous phase transition upon heating. To further study the existence of the loosely packed LLSs and to probe the structural stability, we performed simultaneous SAXS/WAXS study during heating, summarized in Fig. 4. At temperatures above $T_x \sim 633\text{ K}$, crystallization occurs in the ED $\text{Ni}_{82}\text{P}_{18}$ sample as evidenced by the abrupt appearance of Bragg peaks in the diffraction data, see inset of Fig. 4a. Meanwhile, the SAXS scattering intensity increases when heating above $\sim 633\text{ K}$. No noticeable changes in the SAXS profiles were found before crystallization. However, an interference peak⁴⁰ in the ED $\text{Ni}_{82}\text{P}_{18}$ sample appeared after crystallization, and its intensity continuously increases during heating.

Figure 4b shows the plots for the SAXS integrated intensity at a Q range of $0.0049\text{--}0.1\text{ \AA}^{-1}$ and the WAXS integrated intensity at a Q range of $5.0191\text{--}5.0253\text{ \AA}^{-1}$. The DSC scan of the ED $\text{Ni}_{82}\text{P}_{18}$ alloy is superimposed, which recorded a heat release at $T_s \sim 450\text{ K}$. The SAXS intensity shows a decrease at temperatures above

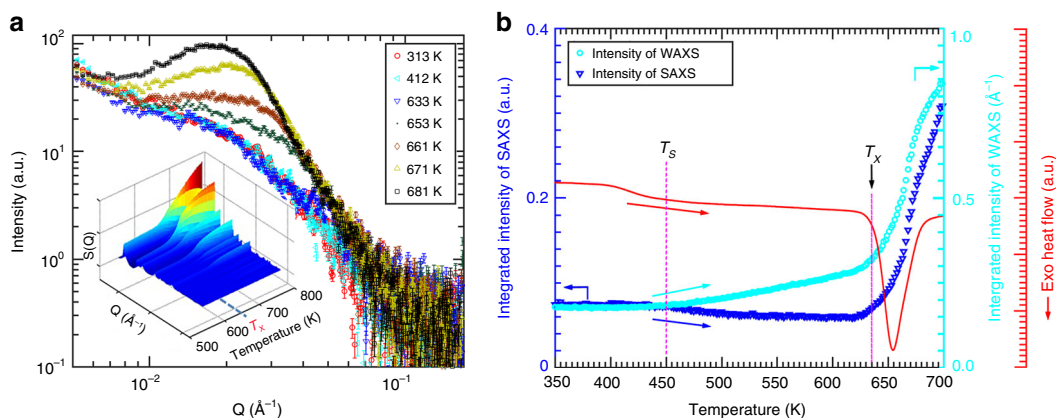


Fig. 4 ‘Solidification-like’ behavior upon heating. **a** Synchrotron small-angle X-ray scattering (SAXS) profiles for the electrodeposition (ED) $\text{Ni}_{82}\text{P}_{18}$ alloy during heating. The inset shows the 3D plot of wide-angle X-ray scattering (WAXS) patterns acquired simultaneously during heating. A rapid development of SAXS intensity is observed above the crystallization temperature of $T_x \sim 633$ K. Error bars are defined as the standard deviation of photon count. **b** The turquoise circles are the normalized integrated intensity of WAXS patterns over Q range, $5.5007\text{--}5.5056 \text{ \AA}^{-1}$. The blue triangles are the normalized integrated intensity of SAXS patterns over Q range, $0.049\text{--}0.1 \text{ \AA}^{-1}$. The red line is the differential scanning calorimetry (DSC) scan of ED sample heating from room temperature to 700 K. The red dotted lines indicate the transition temperature T_S and crystallization temperature T_x . The heating rate for the simultaneous SAXS/WAXS measurement and the DSC scan is 10 K min^{-1}

$\sim T_S$ and a sharp increase at T_x . The decrease of the SAXS intensity is attributed to a reduction in the degree of the nano-scale heterogeneity above $\sim T_S$. Conversely, the WAXS intensity shows an increase upon heating above $\sim T_S$. Taken together, these results indicate an accelerated ordering with reduced heterogeneity at these temperatures, which is similar to the behavior of a solidification process of MGFLs upon cooling^{41,42}. Supplementary Fig. 8 indicates that the WAXS intensity increases during a real solidification process for the Vit 106 MGFL. The DSC scan for the ED $\text{Ni}_{82}\text{P}_{18}$ alloy is consistent with the ‘solidification-like’ scenario. However, as shown in Fig. 1a, there is no such heat release process for the MG $\text{Ni}_{82}\text{P}_{18}$ at the temperature of $\sim T_S$. All the data presented indicate that there is an accelerated local ordering upon heating due to the existence of abundant loosely packed LLSs. Furthermore, the WAXS patterns upon heating also rule out that crystallization occurs at $\sim T_S$. Supplementary Fig. 9 shows the HRTEM results for ED $\text{Ni}_{82}\text{P}_{18}$ when heating above 600 K (between T_S and T_x), and present an additional confirmation of the amorphous nature of ED Ni–P alloys in this temperature range. These results indicate that the LLS is a metastable structure, which continues to settle during heating. Moreover, the TEM and diffraction results confirmed that the crystallization of MG $\text{Ni}_{82}\text{P}_{18}$ sample (not shown here) starts already at ~ 580 K, a much lower temperature, confirming the better thermal stability of the ED $\text{Ni}_{82}\text{P}_{18}$ alloy compared to the MG $\text{Ni}_{82}\text{P}_{18}$ alloy.

Real space structure analysis and negative thermal expansion.

Figure 5 shows the structure evolution in real-space for ED $\text{Ni}_{82}\text{P}_{18}$ and MG $\text{Ni}_{82}\text{P}_{18}$ alloys upon heating. Figure 5a, b are $G(r)$ profiles for ED and MG $\text{Ni}_{82}\text{P}_{18}$ samples, respectively. Arrows indicate the first R_1 and third R_3 coordination shells. The differential $G(r)$ profiles for both samples, as shown in Supplementary Fig. 10a, b, were obtained by subtracting the first pattern at room temperature. By tracking the position change of R_1 and R_3 for both samples, the structure evolution at short-range and medium-range length scales can be visualized. As shown in Fig. 5c, the peak position of R_1 increases, as expected from the results of thermal expansion measurements. However, the peak position of R_3 decreases, showing a contraction upon heating. As indicated by the arrow in Supplementary Fig. 10a, the behavior of the higher coordination shells beyond R_3 is similar to that of R_3

during heating. For comparison, the peak positions of R_1 and R_3 for MG $\text{Ni}_{82}\text{P}_{18}$ samples were also plotted in Fig. 5d. Both are expanding during heating, as expected.

Figure 6 presents the thermal expansion data for ED and MG $\text{Ni}_{82}\text{P}_{18}$ alloys. The MG $\text{Ni}_{82}\text{P}_{18}$ exhibits a linear expansion upon heating. However, the ED $\text{Ni}_{82}\text{P}_{18}$ shows an anomalous expansion behavior at $\sim T_S$ during heating. The CTE of the ED $\text{Ni}_{82}\text{P}_{18}$ decreases below T_S and approaches the lowest value of $\sim -3 \times 10^{-6} \text{ K}^{-1}$, before starting to increase. The valley in the CTE curve for the ED $\text{Ni}_{82}\text{P}_{18}$ amorphous alloy is exactly at the temperature $\sim T_S$. This anomalous thermal expansion behavior is an additional confirmation of the PPT at T_S , consistent with the thermal contraction of the atomic structure at MRO for ED $\text{Ni}_{82}\text{P}_{18}$ measured by synchrotron X-ray diffraction, as illustrated in Fig. 5c.

Discussion

One of the challenges in order to prove the existence of the PPT is whether kinetically stabilized polyamorphous structures can co-exist. $\text{Ni}_{82}\text{P}_{18}$ amorphous alloys with a nanometer-sized microstructure (called ED $\text{Ni}_{82}\text{P}_{18}$ alloys), characterized by two sub-peaks in the second maximum of structure factor, can be prepared by changing the pulse current density based on ED (Supplementary Fig. 1)^{20,23,43}. The ED $\text{Ni}_{82}\text{P}_{18}$ alloys were found to contain LLSs with abundant loosely packed regions of increased free volume. The main evidence is revealed by the differential PDF, as the higher-order coordination shells show larger distance between atomic pairs, $\sim 2.3\%$ larger relative to the MG counterparts, which is similar to the situation of ‘real’ MGFLs as compared to their glass states. The volume fraction of LLSs in ED $\text{Ni}_{82}\text{P}_{18}$ alloys was found to be $\sim 50\%$ by SAXS measurements, consistent with TEM observations. As shown in Fig. 1, although EDS mapping and 3D APT mapping did not resolve noticeable compositional variations at the nanoscale, HAADF in STEM mode showed bright/dark regions, indicating the existence of phases with different densities. The phases with smaller density appear as dark regions in the HAADF images because of their lower density, potentially leading to faster polishing during the thinning process of TEM sample^{44,45}. In summary, the experimental results confirm the coexistence of two amorphous phases with comparable volume fractions but different packing schemes at MRO in ED $\text{Ni}_{82}\text{P}_{18}$ alloys.

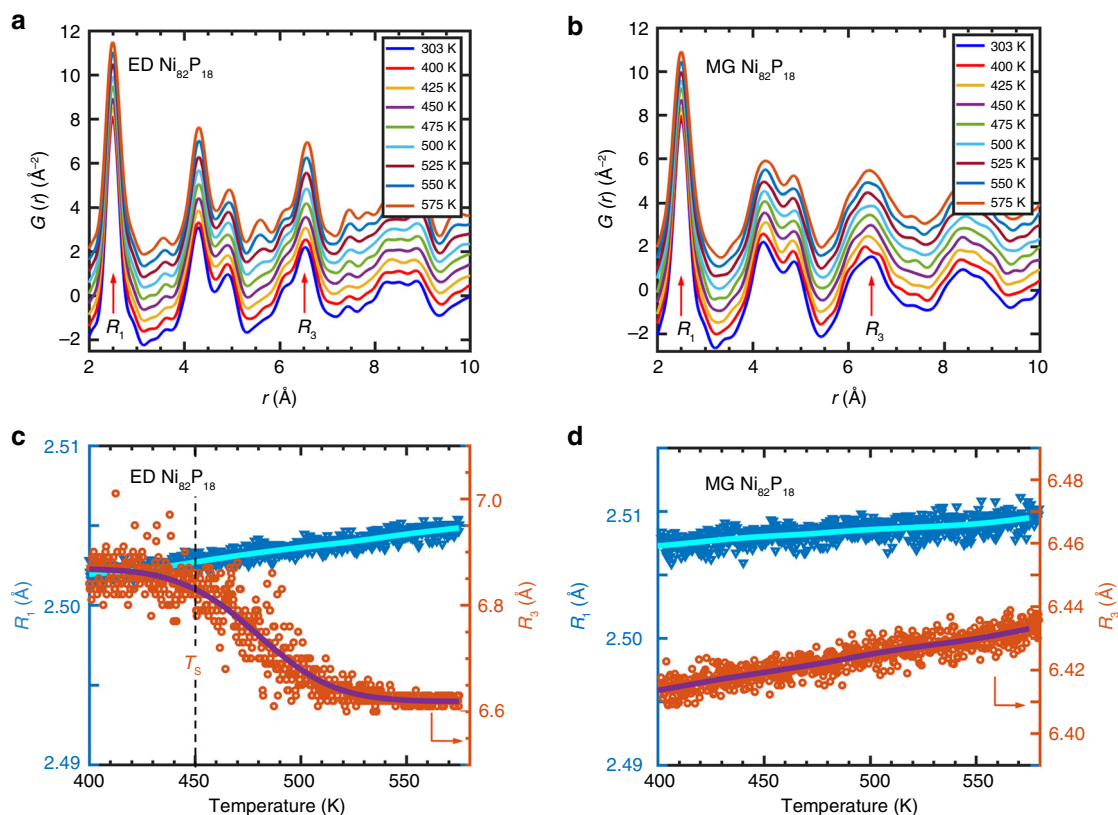


Fig. 5 Real-space structure analysis. **a** Reduced pair distribution function (PDF), i.e., $G(r)$ obtained by fast Fourier transform of the structure factor, profiles during the heating process for the electrodeposition (ED) $\text{Ni}_{82}\text{P}_{18}$ alloy. The arrows indicate the first coordination shell (R_1) and the third coordination shell (R_3). **b** The temperature-dependent reduced pair distribution function, $G(r)$ of the metallic glass (MG) $\text{Ni}_{82}\text{P}_{18}$ alloy. **c** The peak positions of R_1 and R_3 as a function of temperature. The peak position of R_1 shows normal expansion upon heating, but the R_3 peak position shows an anomalous contraction upon heating and exhibits a crossover at T_S . **d** The position of the first coordination shell, R_1 , and the third coordination shell, R_3 , as a function of the temperature of the MG $\text{Ni}_{82}\text{P}_{18}$ alloy

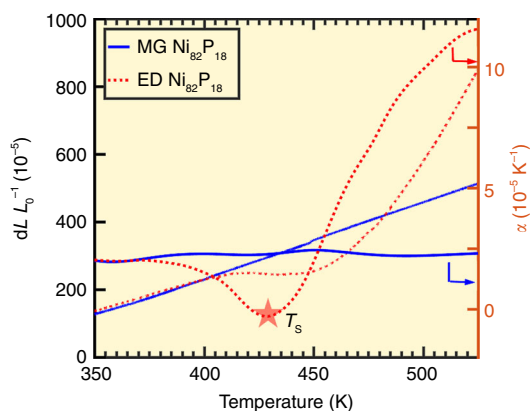


Fig. 6 Anomalous thermal expansion behaviors. The blue curves are the relative displacements and the corresponding coefficients of thermal expansion for metallic glass (MG) $\text{Ni}_{82}\text{P}_{18}$ samples as a function of temperature, during tension using thermal mechanical analysis (TMA). The red dotted lines are the relative displacements and the corresponding coefficients of thermal expansion for electrodeposition (ED) $\text{Ni}_{82}\text{P}_{18}$ samples as a function of temperature, during tension using TMA. The MG sample exhibits a linear expansion upon heating, while the ED sample shows an anomaly. The coefficient of thermal expansion is almost zero, at temperature $\sim T_S$, as indicated by the star

Due to the presence of LLSs, the ED $\text{Ni}_{82}\text{P}_{18}$ alloys exhibit a ‘solidification-like’ accelerated local ordering upon heating. As shown by the SAXS/WAXS experimental data in Fig. 4, the structure change for the ED $\text{Ni}_{82}\text{P}_{18}$ alloys at T_S is similar to the one for the real metallic liquids at T^* , a liquid–liquid phase transition (LLPT) temperature (Supplementary Fig. 8), i.e., at medium-range length scale. The ‘solidification-like’ ordering process upon heating is likely due to the relaxation of the local structure by the fast dynamics in the LLS and the annihilation of excessive free volume. Hyperquenched MGs^{46,47} and nanostructured Sc–Fe nanoglass³⁸ prepared by inert gas condensation (IGC) were reported to have an excess free volume. Glasses prepared by these two processing routes are characterized by an enthalpy release peak below the glass transition, which is similar to the anomalous heat release process at T_S for the ED $\text{Ni}_{82}\text{P}_{18}$ alloys upon heating. A structure transition temperature at ~ 430 K has been proposed in $\text{Ni}_{81}\text{P}_{19}$ glasses³², which varies by 20 K from the T_S , ~ 450 K observed in the present study. The difference may be caused by the composition difference and/or the different sample production conditions, such as quenching temperature³¹. Recently, a cluster ordering process scenario has been proposed to explain the free volume annihilation process for hyperquenched MGs and Sc–Fe nanoglass prepared by IGC^{38,46,47}. Thus, the structural change at $\sim T_S$ observed in the present study suggests that the anomalous thermal behavior of $\text{Ni}_{82}\text{P}_{18}$ at T_S is analogous to a transition from ‘LLS-to-SLS’ upon heating.

The anomalous thermal contraction of ED Ni₈₂P₁₈ at higher coordination shells provided further evidence of the existence of a LLS at room temperature and suggested that the ED Ni₈₂P₁₈ alloys have controllable MRO structure. The transition point during the thermal contraction is at $\sim T_S$. The thermal contraction for the ED Ni₈₂P₁₈ sample at the MRO is consistent with the structural features of the LLS as discussed earlier. The unusual change in the MRO structure in ED Ni₈₂P₁₈ further indicates that there is a PPT from a less dense LLS to a denser SLS. The CTE measurements have often been used to identify ‘first-order’ phase transitions in condensed matter^{48–50}. The anomalous change of CTE of the ED Ni₈₂P₁₈ amorphous alloy by the TMA measurements confirmed the PPT at $\sim T_S$, as shown in Fig. 6. The thermal expansion of the ED Ni₈₂P₁₈ shows a transition point at T_S , where the CTE of ED Ni₈₂P₁₈ alloy is \sim zero. Upon heating to $\sim T_S$, the SLS in ED Ni₈₂P₁₈ alloy shows thermal expansion, while the LLS shows a contraction. The cancellation of the positive and negative thermal expansions by different phases could result in a \sim zero thermal expansion in ED Ni₈₂P₁₈ amorphous alloys. By changing the volume fraction of the SLSs and LLSs with varied MRO, it is possible to design amorphous alloys with tailorable thermal expansion behavior.

The crystallization temperature (T_{X2}) of the ED Ni₈₂P₁₈ amorphous alloy is higher than that (T_{X1}) of the MG Ni₈₂P₁₈ amorphous alloy, suggesting higher stability of the ED amorphous alloys. Furthermore, it was also found by additional in situ diffraction studies (not shown here) that, at the same annealing temperature, the time to crystallization in the ED Ni₈₂P₁₈ amorphous alloy is much longer than that in the MG Ni₈₂P₁₈ alloy. As shown in Supplementary Fig. 11, although the final crystalline products are identical (Fig. S3) for both alloys, the structure of the ED Ni₈₂P₁₈ alloy at medium-range scale (e.g., ~ 5.57 Å) starts to relax before crystallization. However, there is no such relaxation process for the MG Ni₈₂P₁₈ alloy. The relaxation of before crystallization also means that ED samples are more stable. Recently, a thermodynamic scenario for nanostructured glasses prepared by IGC has been proposed, where the free energy of the interfacial regions between the MG particles are described as a lower energy amorphous state compared to the MG state⁵¹. It has been shown that the MGs after the occurrence of LLPT often showed better stability^{28,30,52}. These studies suggested that it is easier for the amorphous structure to approach the lowest energy state after relaxation^{53–55}.

These structural differences can lead to a dramatic change in other macroscopic properties. Here we also would like to point out that the differences in structure and changes upon annealing also result in differences in the mechanical properties of these alloys, with ED Ni₈₂P₁₈ alloys displaying improved ductility. As shown in Supplementary Fig. 12 and Supplementary Note 2, in situ TEM tensile tests for MG Ni₈₂P₁₈ and ED Ni₈₂P₁₈ alloys were conducted at room temperature. The MG Ni₈₂P₁₈ is relatively brittle while the ED Ni₈₂P₁₈ shows an improved tensile ductility. The structural origin of this difference could be attributed to the coexistence of LLSs and SLSs of comparable volume fractions in the ED alloy, which do not exist in the MG alloy. Therefore, the unique microstructure in the ED Ni₈₂P₁₈ alloy may play an important role in the supercooled-liquid-like deformation behavior^{56,57} observed in this material.

In conclusion, the coexistence of liquid-like and SLSs with comparable volume fractions but different packing schemes at medium-range length scale has been established in ED Ni₈₂P₁₈ amorphous alloys, using calorimetry, electron microscopy, PDF analysis, and simultaneous SAXS/WAXS during heating. The ED Ni₈₂P₁₈ alloy possesses a unique structure factor featuring two distinct maxima intensities in the region of the second diffraction peak, both of comparable diffraction intensity. The loosely packed

LLS within these regions was characterized by a larger atomic spacing at medium-range length scale, as revealed by the differential PDF profile. The observed structure change at temperature $\sim T_S$ provides evidence of an ‘LLS-to-SLS’ transition upon heating. The anomalous thermal expansion behavior, contracting at MRO and nearly zero CTE at T_S , is consistent with the scenario of a polyamorphous phase transition at $\sim T_S$, indicating that the ED Ni–P alloys have tailorable MRO. Moreover, the ED Ni–P amorphous alloys have better thermal stability against crystallization and exhibit improved tensile ductility. These results suggest strategies to tailor the macroscopic properties of amorphous alloys, via MRO structural engineering, through the use of ED techniques.

Methods

Sample preparation. ED Ni₈₂P₁₈ alloys were prepared using a multi-phase pulsed ED method. The bath compositions contain 200 g L⁻¹ NiSO₄·6H₂O, 25 g L⁻¹ NiCl₂·6H₂O, and 15 g L⁻¹ H₃PO₃. Boric acid (H₃BO₃) was added as supporting electrolytes and pH buffer. The ED was carried out at 60 °C and pH = 1.2. The applied voltage was varied during the ED process in the form of three steps. During the first step, a high current density of 400 mA cm⁻² was applied for $t_{on1} = 1$ ms. The second step consisted of the application of a lower current density (50–400 mA cm⁻²) for $t_{on2} = 19$ ms. During the third and last step, the current was turned off for $t_{off} = 20$ ms. This procedure was repeated for the total deposition time of 1–3 h. Supplementary Fig. 1 shows the structure factor patterns for different alloys prepared using different current densities. For additional details, we refer to Guo et al.²⁰ MG Ni₈₂P₁₈ ribbons with the same composition as ED Ni₈₂P₁₈ alloys were prepared using melt-spinning with a wheel speed of ~ 30 m s⁻¹ under high-purity argon atmosphere, on to a single copper wheel at 4000 r.p.m.

Transmission electron microscopy. TEM foils are prepared using the twin-jet electropolishing method. The instrument for electropolishing is the automatic twin-jet electro-polisher (Fischione Model 110). The electrolyte using for electropolishing is 16% perchloric acid, 42% acetic acid, and 42% methanol. Polishing parameters are set as voltage ~ 20 V, and current is ~ 40 mA. The electropolishing was performed at ~ 233 K. Details of the TEM sample preparation using electropolishing can also refer to refs.^{44,45}. FEI TF 20 high-resolution TEM (high voltage 200 kV) was employed. Drift-correction mode during EDS mapping in HAADF/STEM mode was used to eliminate the experimental error. The nano-probe with resolution ~ 1 nm was used for EDS mapping.

Differential scanning calorimetry. The DSC curves during heating were measured using platinum crucibles with Netzsch DSC 404 F3 in a high-purity Ar atmosphere. The weight of the samples for DSC is ~ 20 mg. The heating rate is 10 K min⁻¹.

PDF analysis. Synchrotron high-energy X-ray experiments for PDF analysis were conducted at beamline 11-ID-C at the Advanced Photon Source, Argonne National Laboratory. High energy X-rays with a beam size of 0.5 mm \times 0.5 mm and wavelength of 0.10804 Å were used in transmission geometry for data collection. Two-dimensional (2D) diffraction patterns were obtained using a Perkin Elmer amorphous silicon detector. The data acquisition time for each pattern is 1 s. In situ heating was performed using a Linkam TS 1500 stage purified by high-purity Argon flow. A graphite crucible was employed for X-ray diffraction measurements of high-temperature melts. To improve the statistics of the data, 100 patterns were acquired for data averaging. The static structure factor, $S(Q)$ with $Q_{max} \sim 30$ Å⁻¹, was derived from the scattering data by masking bad pixels, integrating images, subtracting the appropriate background and correcting for oblique incidence, absorption, multiple scattering, fluorescence, Compton scattering, Laue correction using Fit2D and PDFgetX2.

Simultaneous SAXS/WAXS. Simultaneous SAXS/WAXS experiments were performed at the beamline 1-ID-E at the Advanced Photon Source, Argonne National Laboratory. A conventional SAXS/WAXS detector array was used. High-energy X-rays with a beam size of 0.1 mm \times 0.1 mm and wavelength of 0.17711 Å were used in transmission geometry for data collection. Two-dimensional (2D) diffraction patterns were obtained using four combination GE detectors. A 2D PIXRAD detector was used for SAXS measurements. In situ heating was performed using a Linkam TS1500 stage with purification by high purity Argon flow. The heating rate is ~ 10 K min⁻¹. The data acquisition time for each pattern is 1 s. However, including the time for saving data, the total acquisition time is ~ 5 s for each pattern. The static structure factor, $S(Q)$ with Q range from 2 to 15.5 Å⁻¹, was derived from the scattering data by masking bad pixels, integrating images, subtracting the appropriate background and correcting for oblique incidence, absorption, multiple scattering, fluorescence, Compton scattering, Laue correction using Fit2D and PDFgetX2. SAXS profiles with Q range from 0.0049 to 0.1686 Å⁻¹

were reduced with data corrected for empty cell scattering, transmission, and detector response using a beamline MATLAB script.

In situ TEM tensile tests. In situ TEM tensile test was conducted using the Hysitron PI 95 TEM Pico-Indenter. The T-shaped specimens were prepared from the ED and MG Ni₈₂P₁₈ parent body by focused-ion-beam (FIB). The sample evolution during the tests was recorded in movies. The methods for details can refer to the Tian et al.⁵⁸. A total of 10 specimens were tested to confirm the observed tensile plasticity of NG Ni₈₂P₁₈ alloys.

Thermal expansion. Thermal expansion measurements were conducted in tensile mode using NETZSCH TMA 402F3. The sample is 15, 5, and 0.035 mm in length, in width, and in thickness, respectively. Before the experiment of the Ni–P samples, a standard sample, Al₂O₃, was employed for calibration of the instrument. Subsequently, a pre-set load force of 0.010 N was applied during the entire test with a nitrogen flow at a flow rate of 20 ml min⁻¹. The heating rate was 20 K min⁻¹, over a temperature range of 303–723 K.

Data availability

The data that support the findings of this study are available from the corresponding author upon request.

Received: 8 February 2019; Accepted: 13 August 2019;

Published online: 27 September 2019

References

- Angell, C. A. Glass-formers and viscous liquid slowdown since David Turnbull: enduring puzzles and new twists. *MRS Bull.* **33**, 544–555 (2008).
- Miracle, D. B. A structural model for metallic glasses. *Nat. Mater.* **3**, 697–702 (2004).
- Weintraub, H. et al. Through the glass lightly. *Science* **267**, 1609–1618 (1995).
- Sheng, H. W., Luo, W. K., Alamgir, F. M., Bai, J. M. & Ma, E. Atomic packing and short-to-medium-range order in metallic glasses. *Nature* **439**, 419–425 (2006).
- Berthier, L. & Biroli, G. Theoretical perspective on the glass transition and amorphous materials. *Rev. Mod. Phys.* **83**, 587–645 (2011).
- Plummer, J. & Johnson, W. L. Is metallic glass poised to come of age? *Nat. Mater.* **14**, 553–555 (2015).
- Ma, E. Tuning order in disorder. *Nat. Mater.* **14**, 547–552 (2015).
- Chen, M. W. A brief overview of bulk metallic glasses. *NPG Asia Mater.* **3**, 82–90 (2011).
- Peker, A. & Johnson, W. L. A highly processable metallic glass: Zr_{41.2}Ti_{13.8}Cu_{12.5}Ni_{10.0}Be_{22.5}. *Appl. Phys. Lett.* **63**, 2342–2344 (1993).
- Ma, D., Stoica, A. D. & Wang, X. L. Power-law scaling and fractal nature of medium-range order in metallic glasses. *Nat. Mater.* **8**, 30–34 (2009).
- Mattern, N., Stoica, M., Vaughan, G. & Eckert, J. Thermal behaviour of Pd₄₀Cu₃₀Ni₁₀P₂₀ bulk metallic glass. *Acta Mater.* **60**, 517–524 (2012).
- Mauro, N. A., Blodgett, M., Johnson, M. L., Vogt, A. J. & Kelton, K. F. A structural signature of liquid fragility. *Nat. Commun.* **5**, 4616 (2014).
- Kelton, K. F. et al. First x-ray scattering studies on electrostatically levitated metallic liquids: demonstrated influence of local icosahedral order on the nucleation barrier. *Phys. Rev. Lett.* **90**, 195504 (2003).
- Hirata, A. et al. Geometric frustration of icosahedron in metallic glasses. *Science* **341**, 376–379 (2013).
- Klement, W., Willens, R. H. & Duwez, P. Non-crystalline structure in solidified gold–silicon alloys. *Nature* **187**, 869–870 (1960).
- Brenner, A., Couch, D. E. & Williams, E. K. Electrodeposition of alloys of phosphorus with nickel or cobalt. *J. Res. Natl Bur. Stand.* **44**, 109–122 (1950).
- Djokic, S. S. Electrodeposition of amorphous alloys based on the iron group of metals. *J. Electrochem. Soc.* **146**, 1824–1828 (1999).
- Pillai, A. M., Rajendra, A. & Sharma, A. K. Electrodeposited nickel–phosphorous (Ni–P) alloy coating: an in-depth study of its preparation, properties, and structural transitions. *J. Coat. Technol. Res.* **9**, 785–797 (2012).
- Bakonyi, I. et al. Magnetic properties of electrodeposited, melt-quenched, and liquid Ni–P alloys. *Phys. Rev. B* **47**, 14961–14976 (1993).
- Guo, C. Y. et al. Ni–P nanoglass prepared by multi-phase pulsed electrodeposition. *Mater. Res. Lett.* **5**, 293–299 (2017).
- Zoikis-Karathanasis, A., Pavlatou, E. A. & Spyrellis, N. Pulse electrodeposition of Ni–P matrix composite coatings reinforced by SiC particles. *J. Alloy. Compd.* **494**, 396–403 (2010).
- Steeb, S. & Lamparter, P. Structure of binary metallic glasses. *J. Non-Cryst. Solids* **156–158**, 24–33 (1993).
- Calvo-Dahlborg, M., Machizaud, F., Nhien, S., Vigneron, B. & Dahlborg, U. Structural study of a phase transition in a NiP metallic glass. *Mater. Sci. Eng.* **A226–228**, 197–203 (1997).
- Sheng, H. W. et al. Polyamorphism in a metallic glass. *Nat. Mater.* **6**, 192–197 (2007).
- Fedotov, V. K. et al. Solid-state amorphization of a quenched high-pressure GaSb phase studied by real-time neutron diffraction: evolution of the crystalline phase. *J. Phys.-Condens. Mater.* **21**, 045402 (2009).
- Calvo-Dahlborg, M. et al. Neutron scattering study of bulk amorphous GaSb. *J. Non-Cryst. Solids* **244**, 250–259 (1999).
- Antonov, V. E. et al. Phase transformations of the amorphous Zn–Sb alloy under high pressures. *Int. J. High Press. Res.* **17**, 261 (2000).
- Xu, W. et al. Evidence of liquid–liquid transition in glass-forming La₅₀Al₅Ni₁₅ melt above liquidus temperature. *Nat. Commun.* **6**, 7696 (2015).
- Wei, S. et al. Liquid–liquid transition in a strong bulk metallic glass-forming liquid. *Nat. Commun.* **4**, 2083 (2013).
- Lan, S. et al. Hidden amorphous phase and reentrant supercooled liquid in Pd–Ni–P metallic glasses. *Nat. Commun.* **8**, 14679 (2017).
- Dahlborg, U. & Calvo-Dahlborg, M. Influence of the production conditions on the structure and the microstructure of metallic glasses studied by neutron scattering. *Mater. Sci. Eng.: A* **283**, 153–163 (2000).
- Calvo-Dahlborg, M., Dahlborg, U. & Ruppert, J. Influence of superheat before quench on the structure and stability of NiP metallic glasses studied by neutron scattering techniques. *J. Non-Cryst. Solids* **357**, 798–808 (2011).
- Corb, B. W., O’Handley, R. C., Megusar, J. & Grant, N. J. First-order, structural transformations in metallic glasses. *Phys. Rev. Lett.* **51**, 1386–1389 (1983).
- Lo, Y. F., Wang, X. C., Wu, Z. D., Zhou, W. Z. & Kui, H. W. Direct imaging of a first-order liquid–liquid phase transition in undercooled molten Pd–Ni–P alloys and its thermodynamic implications. *J. Non-Cryst. Solids* **472**, 75–85 (2017).
- Chen, H., Krause, J. & Coleman, E. Elastic constants, hardness and their implications to flow properties of metallic glasses. *J. Non-Cryst. Solids* **18**, 157–171 (1975).
- Ilavsky, J. & Jemian, P. R. Irena: tool suite for modeling and analysis of small-angle scattering. *J. Appl. Crystallogr.* **42**, 347–353 (2009).
- Gleiter, H., Schimmel, T. & Hahn, H. Nanostructured solids—from nanoglasses to quantum transistors. *Nano Today* **9**, 17–68 (2014).
- Fang, J. et al. Atomic structure and structural stability of Sc₇₅Fe₂₅ nanoglasses. *Nano Lett.* **12**, 458–463 (2011).
- Dahlborg, U. et al. Temperature and time dependent structure of the molten Ni₈₂P₁₈ alloy by neutron diffraction. *J. Non-Cryst. Solids* **500**, 359–365 (2018).
- Yang, L. et al. Nanoscale solute partitioning in bulk metallic glasses. *Adv. Mater.* **21**, 305–308 (2009).
- Lan, S. et al. Structural crossover in a supercooled metallic liquid and the link to a liquid-to-liquid phase transition. *Appl. Phys. Lett.* **108**, 221907 (2016).
- Wessels, V. et al. Rapid chemical and topological ordering in supercooled liquid Cu₄₆Zr₅₄. *Phys. Rev. B* **83**, 094116 (2011).
- Lu, X. L., Li, Y. & Lu, L. Co-existence of homogeneous flow and localized plastic deformation in tension of amorphous Ni–P films on ductile substrate. *Acta Mater.* **106**, 182–192 (2016).
- Lan, S., Yip, Y. L., Lau, M. T. & Kui, H. W. Direct imaging of phase separation in Pd_{41.25}Ni_{41.25}P_{17.5} bulk metallic glasses. *J. Non-Cryst. Solids* **358**, 1298–1302 (2012).
- Lan, S., Wu, Z. D., Lau, M. T. & Kui, H. W. Crystallization in homogeneous and phase-separated Pd_{41.25}Ni_{41.25}P_{17.5} bulk metallic glasses. *J. Non-Cryst. Solids* **373**, 5–12 (2013).
- Hu, L. N., Zhou, C., Zhang, C. Z. & Yue, Y. Z. Thermodynamic anomaly of the sub-T-g relaxation in hyperquenched metallic glasses. *J. Chem. Phys.* **138**, 174508 (2013).
- Zhu, F. et al. Intrinsic correlation between β-relaxation and spatial heterogeneity in a metallic glass. *Nat. Commun.* **7**, 11516 (2016).
- Ran, S. et al. Phase diagram and thermal expansion measurements on the system URu₂–xFeSi₂. *Proc. Natl Acad. Sci. USA* **113**, 13348–13353 (2016).
- Ahadi, A., Matsushita, Y., Sawaguchi, T., Sun, Q. & Tsuchiya, K. Origin of zero and negative thermal expansion in severely-deformed superelastic NiTi alloy. *Acta Mater.* **124**, 79–92 (2017).
- Pachoud, E., Cumby, J., Lithgow, C. T. & Attfield, J. P. Charge order and negative thermal expansion in V₂OPO₄. *J. Am. Chem. Soc.* **140**, 636–641 (2018).
- Ivanisenko, Y. et al. Structure and properties of nanoglasses. *Adv. Eng. Mater.* **20**, 1800404 (2018).
- Wu, Z. W., Li, M. Z., Wang, W. H. & Liu, K. X. Hidden topological order and its correlation with glass-forming ability in metallic glasses. *Nat. Commun.* **6**, 6035 (2015).
- Lu, K. & Wang, J. On Avrami exponent for crystallization of NiP glass. *Scr. Met. Mater.* **21**, 1185–1188 (1987).

54. Wang, J. Q. et al. The ultrastable kinetic behavior of an Au-based nanoglass. *Acta Mater.* **79**, 30–36 (2014).
55. Cao, C. R. et al. Ultrahigh stability of atomically thin metallic glasses. *Appl. Phys. Lett.* **105**, 095304 (2014).
56. Adibi, S., Branicio, P. S. & Joshi, S. P. Suppression of shear banding and transition to necking and homogeneous flow in nanoglass nanopillars. *Sci. Rep.-Uk* **5**, 15611 (2015).
57. Lu, Y. et al. In-situ atomic force microscopy observation revealing gel-like plasticity on a metallic glass surface. *J. Appl. Phys.* **121**, 095304 (2017).
58. Tian, L. et al. Approaching the ideal elastic limit of metallic glasses. *Nat. Commun.* **3**, 609 (2012).

Acknowledgements

We acknowledge Dr. Lin Tian for the in situ TEM tensile tests. We also would like to give our thanks to Dr. Chellali Mohammed Reda for the APT measurement with the support of the Karlsruhe Nano Micro Facility. We acknowledge Mr. Shu Fu for the Rietveld refinement. This work was supported by the National Natural Science Foundation of China (Grant nos. 51871120, 51520105001, 51571119, 51571170, 51501090), the Natural Science Foundation of Jiangsu Province (Grant no. BK20171425), and the Fundamental Research Funds for the Central Universities (Grant nos. 30919011107, 30915015103, 30916011106). T.F. acknowledges the support from the innovation project, Qing Lan project and the distinguished professor project of Jiangsu province. X.-L.W. is supported by a grant from the Research Grants Council of the Hong Kong Special Administrative Region, China (Project no. CityU 11216215). H.H. is thankful to the Deutsche Forschungsgemeinschaft (DFG) for financial support under HA 1344/30-2. This research used the resources of the Advanced Photon Source, a US Department of Energy (DOE) Office of Science User Facility operated for the DOE Office of Science by Argonne National Laboratory under Contract no. DE-AC02-06CH11357.

Author contributions

S.L., T.F. and X.-L.W. designed the project; C.Y.G. and T.F. prepared the electrodeposited NG Ni-P alloys; S.L. and Y.R. performed synchrotron X-ray diffraction experiments at 11-ID-C of APS, ANL; S.L., X.-L.W. and J.A. performed the simultaneous SAXS/WAXS measurements at 1-ID-E of APS, ANL; S.L. and X.-L.W. analyzed the scattering data; S.L. and W.Z.Z. performed the TEM study; C.Q.P. and T.F. did the thermal expansion tests;

T.F., S.L., X.-L.W. and Y.R. analyzed the TMA data; S.L., T.F., X.-L.W., H.H., C.-T.L. and H.G. wrote the paper. All authors analyzed and reviewed the results and provided input to this paper.

Competing interests

The authors declare no competing interests.

Additional information

Supplementary information is available for this paper at <https://doi.org/10.1038/s42005-019-0222-9>.

Correspondence and requests for materials should be addressed to T.F. or X.-L.W.

Reprints and permission information is available at <http://www.nature.com/reprints>

Publisher's note Springer Nature remains neutral with regard to jurisdictional claims in published maps and institutional affiliations.



Open Access This article is licensed under a Creative Commons Attribution 4.0 International License, which permits use, sharing, adaptation, distribution and reproduction in any medium or format, as long as you give appropriate credit to the original author(s) and the source, provide a link to the Creative Commons license, and indicate if changes were made. The images or other third party material in this article are included in the article's Creative Commons license, unless indicated otherwise in a credit line to the material. If material is not included in the article's Creative Commons license and your intended use is not permitted by statutory regulation or exceeds the permitted use, you will need to obtain permission directly from the copyright holder. To view a copy of this license, visit <http://creativecommons.org/licenses/by/4.0/>.

© The Author(s) 2019